Citation
Liu, Y. and Paskevicius, M. and Sofianos, M.V. and Parkinson, G. and Wang, S. and Li, C.Z. 2021. A SAXS study of the pore structure evolution in biochar during gasification in H2O, CO2 and H2O/CO2. Fuel. 292: ARTN 120384. http://doi.org/10.1016/j.fuel.2021.120384

A SAXS study of the pore structure evolution in biochar during gasification in H_2O, CO_2 and H_2O/CO_2

Yurong Liu[1], Mark Paskevicius[1], M. Veronica Sofianos[1,2], Gordon Parkinson[1], Shuai Wang[1], Chun-Zhu Li[1*]

[1] *Fuels and Energy Technology Institute, Curtin University, GPO Box U1987, Perth, WA 6845, Australia*

[2] *School of Chemical and Bioprocess Engineering, University College Dublin, Belfield, Dublin 4, Ireland*

[*] *Corresponding author: czlicurtin@gmail.com*

Abstract

Gasification of biomass allows for its efficient utilisation as a renewable fuel through syngas production. This work presents the different effects of gasifying agents (H_2O, CO_2 and H_2O/CO_2) on the pore structure evolution in biochar during gasification. The effects of temperature (700, 800 and 900°C) and biomass particle size (up to 5.6 mm) were also studied. The pore structure of biochar was characterized using synchrotron small angle X-ray scattering (SAXS). The pore development in biochar during gasification in H_2O/CO_2 was close to that in H_2O. Carbon removal is more selective in CO_2 than H_2O and the derived biochar displayed pore fractal features, whereas the biochars gasified in H_2O and H_2O/CO_2 exhibited a surface fractal network due to the less selective carbon removal in the presence of H_2O. The pore structure development produced by various gasifying agents was paralleled by the evolution of the aromatic structures characterized by Raman spectroscopy. The different pore structure features result from the different reactivity of carbon sites with H_2O and CO_2, which can be attributed to the different amounts of O-containing groups in biochar, as well as the different reactivity of H_2O and CO_2. Increasing temperature reduced the differences in pore structure between biochars gasified in H_2O and CO_2. Biomass particle size had little impact on the pore structure of biochar.

Keywords: Pore structure, biochar gasification, SAXS, O-containing functional groups, reactivity.

1. Introduction

The ever-increasing need for the reduction of greenhouse gas emissions has made clean and renewable energy resources attractive. Biomass, as a potential carbon-neutral and renewable energy source, has gained particular attention [1,2]. Gasification is a promising technology to achieve highly efficient utilization of biomass by thermochemically converting biomass to syngas, which can be further used for electricity generation and the production of liquid fuels and chemicals [2]. During gasification, carbon atoms are continuously removed by reacting with gasifying agents, leading to the rearrangement and reorganisation of the residual carbon matrix [3]. As the porosity in biochar originates from the disordered organisation of the carbon matrix, therefore, the porous structure of biochar changes drastically in the meantime [4,5]. The study of the changes in the pore structure of biochar is therefore essential for understanding the reaction pathways of biochar during gasification in various gasifying agents.

Moreover, the porous nature of activated biochar is a key property influencing its utilization as an absorbent and possible energy storage material [6]. Therefore, the study of the pore structure of biochar is also of great significance for achieving efficient utilization of biochar as well as for optimizing the process of thermal activation to produce activated carbon.

Intensive studies [7,8,17,18,9–16] have been undertaken on the porosity development of biochar during gasification. It has been widely found that H_2O and CO_2 produce biochars with different pore size distributions. Despite the considerable efforts made by many researchers, the explanation for the different effects of H_2O and CO_2 on the pore development in biochar is not unanimous. Some studies attribute it to the different diffusion coefficients of H_2O and CO_2 arising from their different molecular dimensions [13,19,20]. Others believe that it is the differences in extents of product (H_2 and CO) inhibition in the C—CO_2 and C—H_2O reactions that causes the different porosity development between biochars gasified in H_2O and CO_2 [21,22].

In any case, we believe the porosity development in biochar is a function of the gasification mechanism. During biochar gasification, with continuous carbon removal and re-arrangement of the carbon structure, the pore structure described by the pore shape and size distribution evolves simultaneously [5]. To have a complete picture of the process of biochar gasification or activation, one must have an adequate understanding of the evolution of the pore structure that is a consequence of the alteration of the carbon skeleton, driven by gasification/activation under different conditions. However, as far as we know, hardly anyone has connected the evolution of pore structure in biochar to changes in its chemical structure.

Therefore, it is compelling to investigate the evolution of both the pore structure and chemical structure of biochar during gasification. Small angle X-ray scattering (SAXS) has been demonstrated to be suitable for characterizing the pore structure of disordered carbonaceous materials as it has advantages over other traditional techniques such as gas (i.e. N_2) adsorption/desorption and transmission electron microscopy (TEM) [23]. For example, gas adsorption can only detect the pores that gases can access, and transmission electron

71 microscope (TEM) can only give the information of pores in a limited sample volume [8,24–
72 26]. SAXS can detect a wide range of pore sizes including closed pores in bulk samples
73 [11,27,28]. More importantly, SAXS has an advantage of "seeing" into the structure of the
74 carbon matrix in biochar by giving information on the fractal features of the pore network
75 over different length scales [29–31]. A fractal model is a mathematical method of describing
76 disordered and irregular objects [32,33]. The fractal dimension of pores is particularly useful
77 in describing the network of pore aggregation (pore fractal) as well as the irregularity and
78 roughness of pore boundaries (surface fractal) [34]. Thus, changes in the fractal dimension of
79 pores can describe the evolution of the carbon skeleton in biochar during gasification. On the
80 other hand, FT-Raman spectroscopy has long been demonstrated to be suitable for
81 characterizing the chemical structure of biochar [3,35,36].

82 To this end, in this work, biochar was gasified in H_2O, CO_2 and H_2O/CO_2 respectively to
83 various conversion levels. The evolution of the pore structure and chemical structure was
84 characterized by SAXS and FT-Raman spectroscopy respectively. The aim of this study is to
85 investigate the different mechanisms through which the three gasifying agents develop
86 micro- and mesopores in biochar by combining the fractal properties of the porous structure
87 of biochar with information regarding the transformation of chemical structures in biochar.
88 The effects of temperature and biomass particle size on the pore structure of biochar were
89 also studied.

90 # 2. Experimental

91

92 ## 2.1. Biochar preparation

93

Three different sets of experiments were carried out to prepare the biochar samples. All the biochar samples were prepared using Mallee wood as a feedstock. The Mallee wood has an ultimate analysis of 48.2 wt% C, 6.1 wt% H, 0.2 wt% N and 45.5 wt% O (dry and ash-free basis). The first set (biochar A) was the gasification of biochar (106–250 μm) at 800 ˚C in 15 vol. % H_2O balanced with Ar (designated as H_2O), pure CO_2 (designated as CO_2) and/or 15 vol. % H_2O mixed with CO_2 (designated as H_2O/CO_2) for varying periods (10–50 min). The starting biochar was obtained from the pyrolysis and partial gasification (5–10 min) of Mallee biomass at 750 – 850 °C in our gasification demonstration plant [37,38]. A three-frit two-stage fluidized-bed/fixed bed quartz reactor [35,36] was employed to perform the gasification of biochar. Briefly, 1 g of biochar was preloaded in the middle frit of the reactor before being heated under argon. After the reactor had stabilised at 800 °C, argon was switched to H_2O, CO_2 or H_2O/CO_2 at a total flow rate of 2.0 L min^{-1} to continue the gasification of biochar for different times. Biochar samples were collected after the reactor had cooled down to room temperature under argon flow.

The second set (biochar B) of experiments was the gasification of Mallee wood (4.75–5.6mm) at different temperatures (700, 800 or 900 ˚C) in 15% H_2O/Ar and/or pure CO_2 for the same time (4 min). The experimental procedure was described in our previous study [39]. Briefly, a fluidised-bed quartz reactor was placed in a furnace and heated up with argon flowing through the reactor. After the target temperatures were reached, approximately 2 g of Mallee wood was fed into the reactor to commence the pyrolysis of the sample. The reactor was held for 20 min in argon after the completion of feeding. Afterwards, argon was switched to 15% H_2O/Ar and/or pure CO_2 to proceed the gasification of biochar for 4 min. The reactor was then lifted out of the furnace and cool down to room temperature in argon before the biochar was collected.

The third set (biochar C) of experiments was the gasification of biomass with different particle sizes at 800°C in 15% H_2O/Ar and/or pure CO_2. The particle sizes of Mallee wood samples were: 0.18−1.0, 1.0−2.0, 2.0−3.35, 3.35−4.0, 4.0−4.75, and 4.75−5.6 mm. As described in detail previously [40], a fluidised-bed quartz reactor was firstly heated up to 800°C with 15% H_2O/Ar or pure CO_2 flowing through the reactor. Afterwards, 2 g of Mallee wood was fed into the reactor within 4 min. When the feeding of biomass was finished, the reactor was immediately lifted out of the furnace and cooled down to room temperature in argon. The obtained biochar samples were then collected to study the influence of biomass particle size on the pore structure of biochar.

2.2. Characterisation of the pore structure of biochar

2.2.1. SAXS measurement

The pore structure of biochar was characterised using the SAXS beamline equipped with a Pilatus 1-M detector at the Australian Synchrotron in Melbourne [41]. The full width at half maximum （FWHM） beam size was 240 μm horizontally and 24 μm vertically. Biochar samples were mounted in square holes (4 x 4 mm) in a 2-mm-thick stainless steel plate with Kapton tape covering both sides. All samples were measured at two camera lengths (3343 mm and 959 mm) to achieve a wide q-range (q is the scattering vector $q = (4\pi/\lambda)\sin(\theta/2)$, λ (1.03 Å) and θ are the wavelength and scattering angle) from 0.005 to 1.5 $Å^{-1}$, respectively, which are appropriate to probe a pore diameter ranging approximately from 0.4 to 125 nm. For each sample, 10 scans were acquired across the sample to provide a representative analysis. The data collection time for each scan is 1 second. Silver behenate was used to calibrate the q-scale of the instrument, and glassy carbon (1 mm thick) was used for absolute intensity calibration [42]. A scattering background from Kapton tape was measured and

subtracted from all data sets. The X-ray transmission (T_s) was acquired by recording the incident flux (I_0) and transmitted flux (I_{BS}) using an upstream detector and a detector inside the beamstop respectively.

2.2.2. SAXS data processing and analysis

At first, the measured intensities were background subtracted and then calibrated using glassy carbon before being normalised for sample thickness and finally converted to absolute intensities [42–44]. The effective solid thickness (*d,* cm) of the sample was calculated using:

$$d = -\ln(T_s)/\mu \quad (1)$$

where, μ is the linear adsorption coefficient of the sample, assumed to be purely amorphous carbon with a density of 2.0 g cm^{-3} [43]. The data collected data at two detector positions were then merged together and fitted with the unified model [45] using Irena described in Ilavsky et al [46] within Igor Pro (Wavemetrics). The unified model [45] was applied because it can describe the structural features of complex systems containing several structural levels (displaying multiple size-scale structures). In general, on a log-log plot of $I(q)$, the SAXS spectrum for each level contains a Guinier region (a 'knee-like' feature) and a linear power law region at higher-q [45]. The Guinier region represents the average size of pores and their radius can be calculated by $r = \sqrt{5/3}\ R_g$ (R_g is the radius of gyration of the scattering objects) if we assume the pores are nearly spherical. The slope (P) of the power law region gives information on the characteristics of pore morphology and texture by providing fractal dimensions of the pores [30,32,45]. For a smooth and sharp interface between the pore wall and void, the power-law follows Porod's law and P = 4 [45]. Rough surfaced pores can be represented by surface fractals, where the value of P lies between 3 and 4 and the fractal

dimension $D_s = -P + 6$. The increase of D_s represents an increase in surface roughness. Aggregate-type structures can be explained by pore fractal where $P < 3$ and the fractal dimension $D_p = P$.

In the case of biochar, three structural levels were used to model the scattering curve. As shown in Fig. s1, the three levels represent the scattering from the microporous (1 – high q), mesoporous (2 – middle q) and macroporous (3 – low q) size regimes, respectively. Because the scattering intensity in the high q power law region is too close to the scattering from the background, it was assumed that the micropore surface is smooth and the slope of the high q (level 1) power law was fixed ($P_1 = 4$). This is also necessary to obtain a stable and repeatable fit to the data. Due to the limited q range, a Guinier regime does not present from the macroporous size regime, which would exist at even lower q (< 0.005 $Å^{-1}$). As a result, the third structural level at low q only includes a power law region (P_3). As such, refined parameters, including the average size of micro- and mesopores (given by R_{g1} and R_{g2} respectively) as well as the fractal dimensions (given by P_2 and P_3), were extracted from SAXS data.

The specific surface area for a surface fractal [47] using a particular measurement scale, r, is given by the following (r = 4 Å, the size of a nitrogen molecule in this study, so the results can be comparable with surface areas calculated by N_2 adsorption/desorption isotherms using the Brunauer, Emmett and Teller (BET) method) :

$$S(r) = Sr^{2-D_s} \quad (2)$$

Where S is given by:

$$S = 2\pi\varphi(1-\varphi)B/Q\rho_{bulk}F(D_s) \quad (3)$$

Where $F(D_s)$, φ and Q are given by the following:

$$F(D_s) = \Gamma(5 - D_s)\sin[\pi(3 - D_s)/2]/(3 - D_s) \quad (4)$$

$$\varphi = \rho_{bulk}/\rho_{base\ material} \quad (5)$$

$$Q = \int_0^\infty I(q)q^2 dq = 2\pi^2 G/V_p \quad (6)$$

Where ρ_{bulk} is the bulk density and can be calculated $\rho_{bulk} = \frac{\rho_{base\ material}\ d^3}{{d_{tot}}^3}$ (d and d_{tot} are the effective solid thickness and the total thickness of the sample (0.2 cm), (see ref. [48] for equation formulation), $\rho_{base\ material}$ is the true density of the solid material (2.0 g cm^{-3}), and V_p is the volume of the primary scatterer (pores in this case).

For a mass fractal, the surface area can be determined by the following [32]:

$$\frac{total\ surface\ area}{mass\ sample} = \frac{(S_p/V_p)\varphi}{\rho_{bulk}} = \frac{2\pi^2\varphi_p B_{mass-fractal}}{A\rho_{bulk}Qr^{(4-Dm)}} \quad (7)$$

Where $B_{mass-fractal}$ is the power-law scaling prefactor obtained from the unified fit, r is 4 Å, *A* is the geometric factor and assumed to be 7.6, see details elsewhere [32].

A carbon black standard (used for the calibration of a Micromeritics' TriStar II gas adsorption analyser) was used as a specific surface are (SSA) reference and measured using SAXS. The SSA (S_{SAXS} = 26 ± 0.5 m^2 g^{-1}) obtained from SAXS is comparable to the SSA acquired by N_2 adsorption (S_{BET} = 21.0 ± 0.75 m^2 g^{-1}) but likely also includes some surface area from closed porosity.

Pore size distributions were determined using the IPG/TNNLS (Internal Point Gradient-Total Non-Negative Least Square) fitting method in Irena as can be seen elsewhere [46].

2.3. Characterisation of the chemical structure of biochar

A Perkin–Elmer Spectrum GX FT-IR/Raman was used to characterize the chemical structure of biochar, following the procedure described earlier [3]. In brief, the Raman spectrum (800–1800 cm^{-1}) was baseline-corrected and fitted with 10 Gaussian bands at representative wavenumbers. The assigned G_R (1540 cm^{-1}), V_L (1465 cm^{-1}) and V_R (1380 cm^{-1}) bands represent the small aromatic ring systems with 3–5 rings. The D band (1300 cm^{-1}) corresponds to large aromatic ring systems with 6 or more rings [3]. The band area ratio $I_{(GR+VL+VR)}/I_D$ was used to reflect the transformation of aromatic structures in biochar, where an increase of the ratio represents a growth in the content of large aromatic ring systems (more than 6 rings) [3]. The total Raman peak area was also used to characterize the total O-containing functional groups in biochar.

3. Results and discussion

3.1. Evolution of biochar conversion with time during gasification in H_2O, CO_2 and H_2O/CO_2 at 800°C (biochar A)

The weight losses (conversion level) of biochar samples with increasing gasification/activation time are shown in Fig. 1. It is clearly shown that, after gasification/activation at 800°C for the same time, the biochar gasified in H_2O/CO_2 reaches the highest conversion level followed by the H_2O gasified biochar. The biochar gasified in CO_2 shows the lowest conversion level. This indicates that the simultaneous use of H_2O and CO_2 enhances reaction rate, giving rise to a higher rate of biochar conversion than that in the case of using H_2O or CO_2 alone. It also, in turn, indicates that the reactivity of biochar with H_2O is higher than that with CO_2.

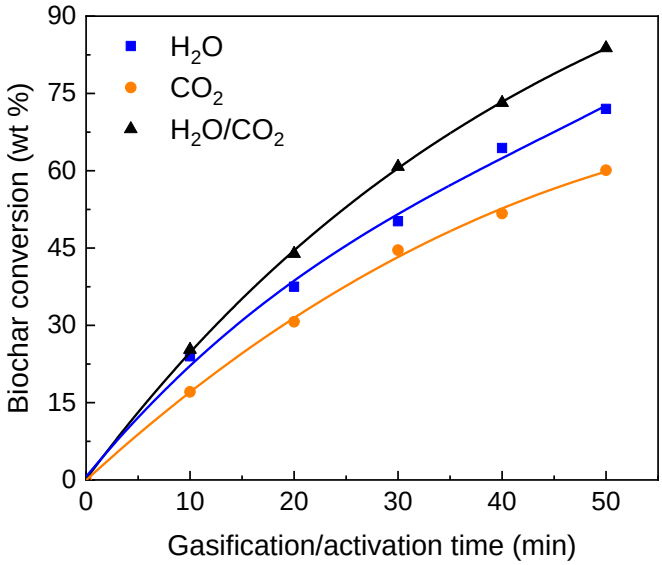

Fig. 1. Biochar conversion as a function of gasification/activation time for biochar samples gasified in H_2O, CO_2 and H_2O/CO_2 at 800°C.

3.2. Evolution of pore structure in biochar during gasification/activation in H_2O, CO_2 and H_2O/CO_2 at 800°C (biochar A)

3.2.1. Evolution of porosity

As stated in our previous work [5], the porosity development during biochar gasification is the result of the creation of micropores and the enlargement of existing pores. New micropores are created by the selective removal of certain carbon atoms by gasifying agents. With the continuous removal of the interior micropore walls, micropores can turn into meso and macropores. The enlargement of pores could also occur when the wall between pores is consumed. These processes take place simultaneously during gasification. Therefore, the observed porosity in biochar at any point is the dynamic balance of pore creation and destruction.

The porosity development of biochar during gasification is paralleled by the evolution of surface area and pore volume with biochar conversion. Fig. 2 shows the development of

SSA as function of biochar conversion level. The values of SSA are similar with those obtained using BET or SSA by others [11,49]. The SSA shows significant growth for both of the H_2O and H_2O/CO_2 gasified biochars, especially in the initial stage of gasification, whereas only a small increase is observed for biochar gasified in CO_2. In general, biochar samples produced by H_2O gasification/activation have a much higher SSA than the CO_2 gasified biochar. The steam gasified biochar achieved the highest SSA of 610 ± 30 $m^2 g^{-1}$ at around 65 wt% conversion before decreasing thereafter when most of the mass was consumed. The H_2O/CO_2 gasification/activation results in similar SSA development to that produced by H_2O gasification/activation.

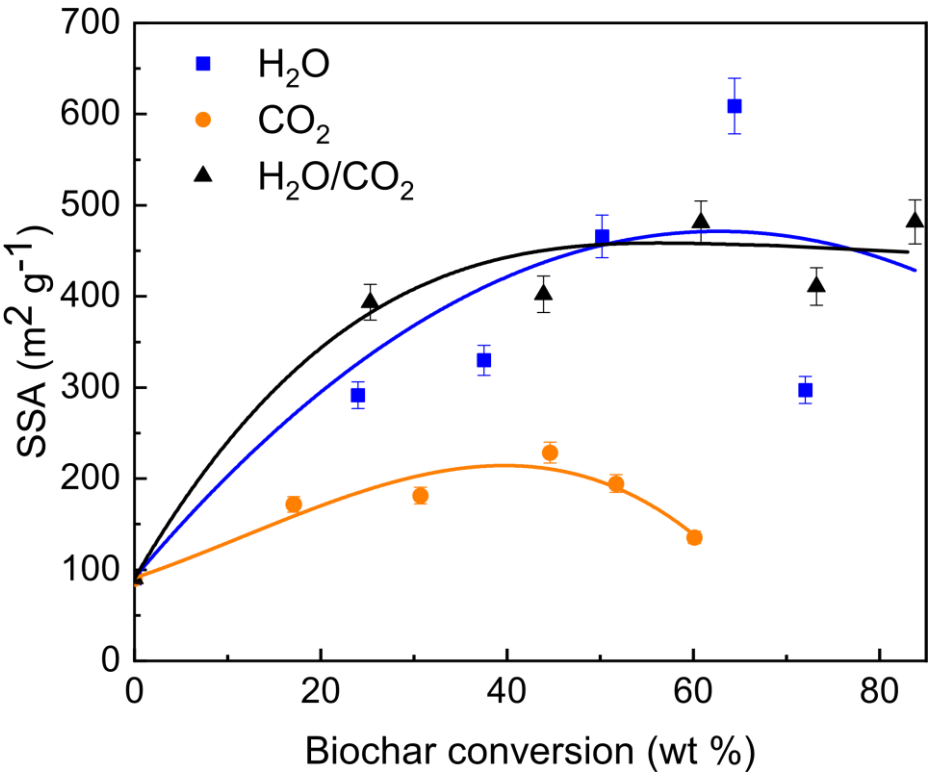

Fig. 2. The SSA of biochar samples gasified in H_2O, CO_2 and H_2O/CO_2 as a function of biochar conversion derived from SAXS data.

Fig. 3 shows the pore size distribution of biochar samples prepared from gasification/activation in (a) H_2O, (b) CO_2 and (c) H_2O/CO_2 for different times (0, 10, 30 50

262 min), giving an overall illustration of porosity development in biochar. A distinct feature of all
263 the biochar samples is that there is an abundance of micropores around 1 Å, showing the
264 highly microporous nature of biochar. Another finding is that, regardless of the gasifying
265 agents, the increase in gasification/activation time (conversion level) leads to a wider pore
266 size distribution biased towards larger pore sizes, suggesting the occurrences of pore
267 enlargement with the continuous removal of carbon throughout the process. Moreover,
268 there is a significant initial increase in micropore volume at the early stages (low conversion)
269 of gasification/activation (especially from 0 to 10 min) followed by a decrease at the late
270 stages. This indicates that the creation of micropores is more marked at lower conversion
271 while the enlargement of micropores become the dominant process at higher conversion.

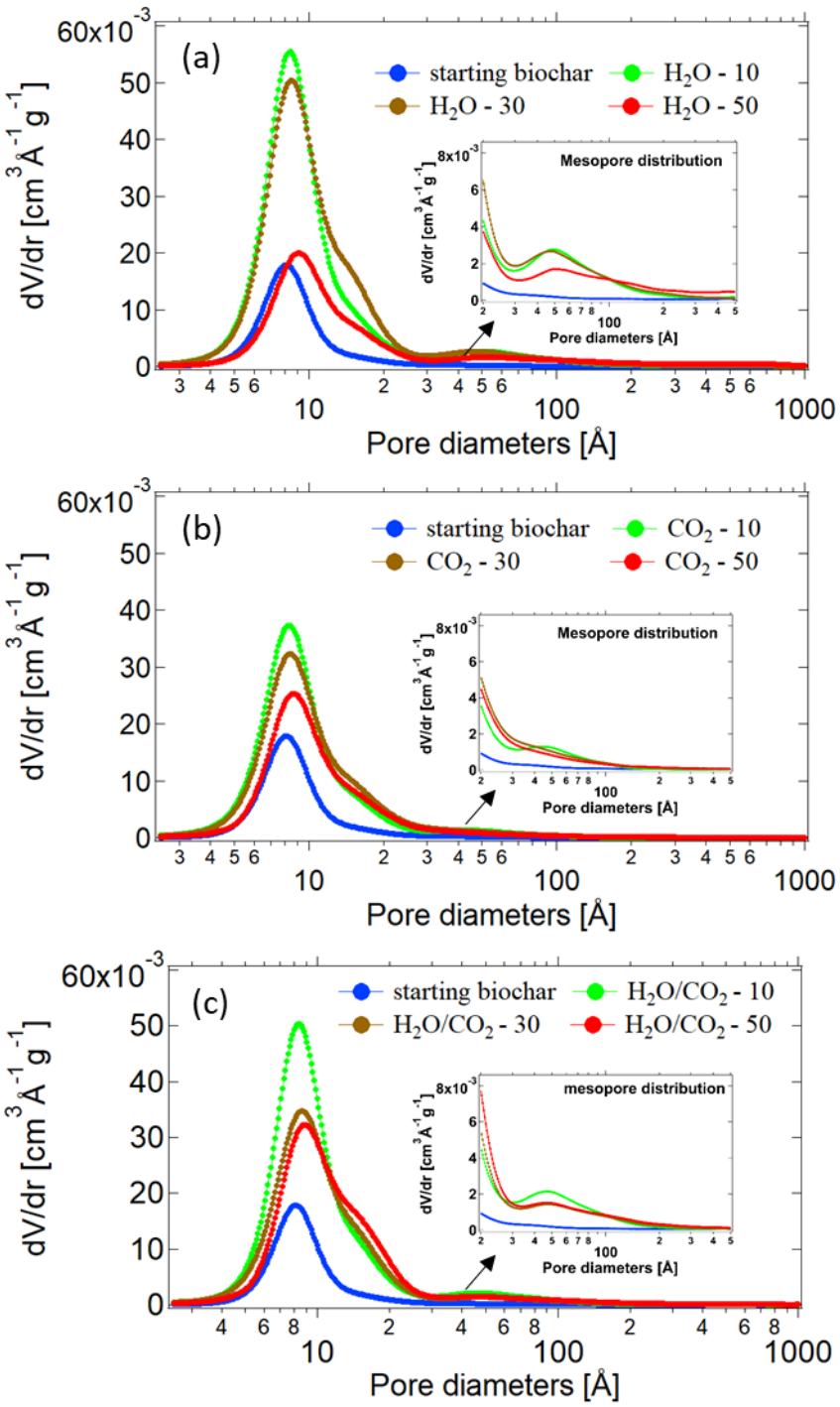

Fig. 3. Pore size distribution obtained from the IPG/TNNLS fitting method to SAXS data for biochar samples gasified in (a) H_2O, (b) CO_2 and (c) H_2O/CO_2 over gasification/activation time (10, 30 and 50 min).

To effectively analyse the creation and destruction of pores during gasification/activation, the micro-and mesopore volume (deduced from the unified fit) were

plotted as a function of biochar conversion and these are included in Fig. 4, where the pore volumes are expressed per g of activated biochar. This can also give a better comparison among different gasifying agents in terms of the differences in porosity development. There is a clear increase in both micro- and mesopore volumes at the early stage of gasification/activation for all the biochar samples gasified in H_2O, CO_2 and H_2O/CO_2. This is also consistent with the size distributions determined earlier. The micropore volume (Fig. 4a) reaches a maximum after a moderate biochar conversion (around 45-50 wt% coversion) before gradually decreasing. However, the reduction in micropore volume is more remarkable for steam gasified biochar than for biochar prepared from gasification/activation in CO_2 and H_2O/CO_2. The mesopore volume (Fig. 4b) exhibits an initial growth until around 40-50 wt% conversion followed by a slight decrease thereafter for biochars gasified in H_2O and H_2O/CO_2. The CO_2 gasified biochar shows a small but steady growth in the mesopore volume up to about 60 wt% conversion. Overall, steam gasification/activation gives rise to the most drastic increase of micro- and mesopore volumes whereas CO_2 gasification/activation leads to the smallest growth. The values of micro- and mesopore volume attained from H_2O/CO_2 gasification/activation are, in general, between the values obtained from the analogous experiments with H_2O and CO_2 separately. Similar results were also reported by others [12,14,15,49,50].

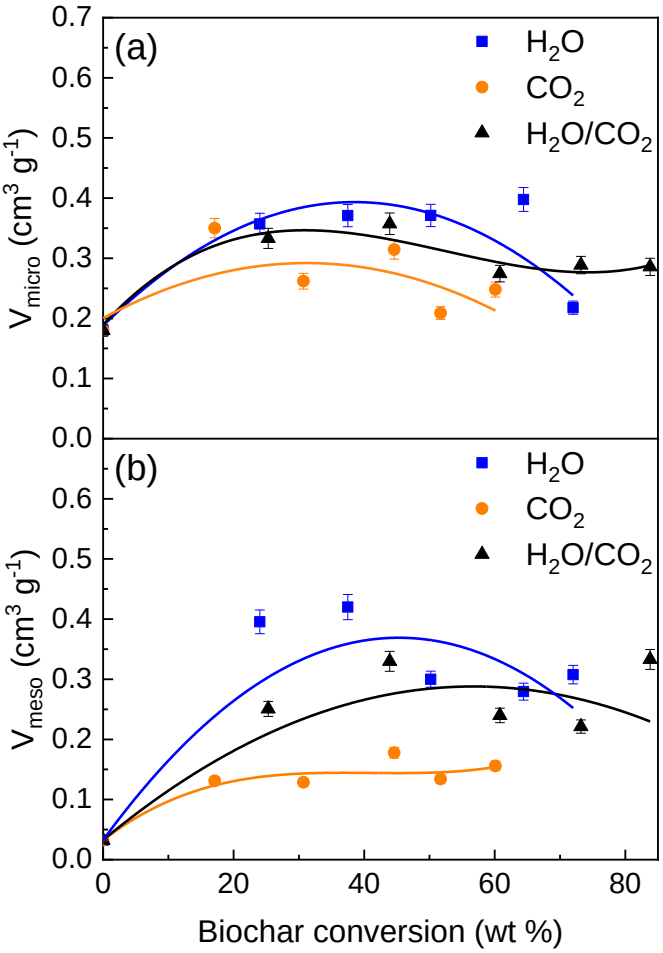

298

299 Fig. 4. Development of (a) micropore volume and (b) mesopore volume as a function
300 of biochar conversion for biochar samples gasified in H_2O, CO_2 and H_2O/CO_2. The results were
301 extracted from the unified fit to SAXS data.

302 The porosity evolution indicates that the creation and enlargement of micropores take
303 place from the onset of gasification/activation, leading to the simultaneous development of
304 micro- and mesopores. Consequently, the micro- and mesopore volumes as well as the SSA
305 increased at the early stages of gasification/activation. At the later stages, the process of
306 micropore enlargement become more predominant, converting micropores to meso and
307 macropores, especially in the case of steam gasification. As a result of pore enlargement, a
308 decrease of micropore volume is accompanied by the growth of mesopore volume. Steam

produced an overall higher mesopore volume in biochar compared with CO_2. It seems that the enlargement of micropores is more remarkable during gasification/activation in H_2O than that in CO_2.

Overall, those observation are in line with our previous results [5] revealed by the *in situ* measurements of the pore development during gasification at 800˚C. It appears that there are no obvious changes in biochar structure during cooling down.

3.2.2. Evolution of pore network

Biochar is a two-phase system consisting of a carbon skeleton formed by disorderly stacked carbon layers as building blocks that surround pores. The carbon layers consist of defective aromatic structures and are often curved/distorted due to the stresses caused by defects and heterogeneous atoms such as O and N. The curved carbon layers are cross-linked and disorderly stacked, leaving empty spaces of different widths and shapes. The empty voids and interlayer spaces are regarded as the porosity [51,52]. When subjected to gasification/activation, the carbon layers undergo a process of continuous re-combination and re-organisation induced by the selective extraction of carbon atoms and other functional groups by gasifying agents. As carbon layers are reorganised there are simultaneous changes in the distance between the layers, the pore size and morphology. Therefore, the evolution of the pore network illustrates the way in which carbon atoms are removed during gasification/activation.

There is no doubt that the pore network in the micropore size regime is the key to understanding the dominant structure of the carbon skeleton. It is also essential to study the pore network in the mesopore size regime in order to have a complete picture of the

evolution pathway of the pore network, especially when considering the transitions from micropore to mesopore and the presence of pore-pore correlations (pore aggregation).

We have previously focussed on the SSA and evolving pore volume from different size regimes. However, it is also important to consider the average pore size and pore morphology in those size regimes. As previously stated, the average pore size is calculated from the radius of gyration in the Guinier regime of the unified fit to SAXS data. Fig. 5 shows the changes of the radius of gyration (R_{g1} and R_{g2} from the average size of micro- and mesopores, respectively) from the unified fits with increasing biochar conversion. In the micropore size regime (high q, level 1), the radius of gyration (R_{g1}) increases gradually for biochar gasified in H_2O, CO_2 and H_2O/CO_2. This indicates a consistent enlargement of micropores during gasification/activation, independent of the gasifying agent. This can be explained by the partial removal of the inner pore walls or the collapse of walls between pores, leading to a growth in the average pore size. At the similar conversion level, the mean micropore size is very close for all biochar samples. This is reasonable given that the molecular size of CO_2 (3.3 Å) and H_2O (2.75 Å) is similar.

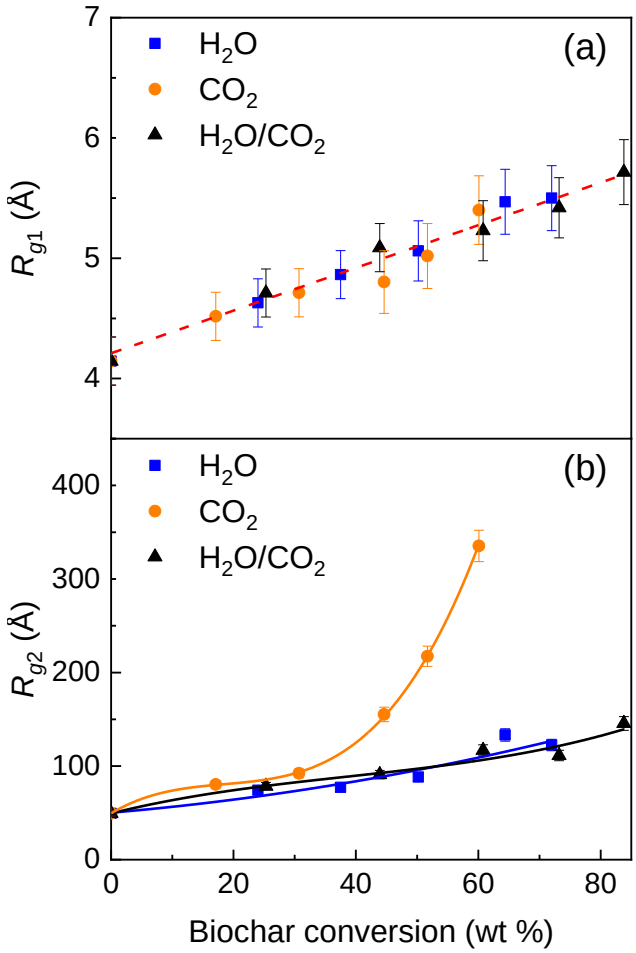

354

355 Fig. 5. Radius of gyration of biochar as a function of biochar conversion in H_2O, CO_2
356 and H_2O/CO_2. (a) R_{g1} and (b) R_{g2} were obtained from micro- (level 1 Guinier region) and
357 mesopore size regime (level 2 Guinier region) of the unified fits to SAXS data.

358 In the mesopore size regime (middle q, level 2), the radius of gyration, R_{g2}, also shows
359 an increasing trend as gasification/activation proceeds. Interestingly, the trends in the case
360 of H_2O and H_2O/CO_2 gasification/activation are similar, whereas CO_2 is markedly different
361 after longer gasification times. After conversion higher that 30 wt%, the increase in R_{g2} during
362 CO_2 gasification/activation (from 90 to 270 Å) is more significant than that during
363 gasification/activation in H_2O and H_2O/CO_2 (from 90 to 120 and 140 Å respectively). The
364 results suggest that the differences in pore development especially in the mesopore size

regime between biochar gasified in H_2O or CO_2 become more significant at higher conversion level.

It is better to analyse the pore network by combining the pore size and the texture and morphology of pores given the possibility of pore aggregation. The pore morphology is characterized by the fractal dimension of the pore network. The fractal dimension allows us to "see" how the pores are arranged/distributed spatially and/or their structural makeup. Surface fractal dimension (*P* lies between 3 and 4) describes the irregularity and roughness of the pore surface, where a dimension of 2 represents a perfectly smooth and sharp interface and a dimension of 3 describes an extremely rough surface. Pore fractals (*P* falls in between 2 and 3) can be viewed as a "negative image" of mass fractals. The dimension of pore fractal describes the space-filling and branching properties of the pore network [30]. A pore fractal where *P* approaches 3 describes an extremely disordered pore network in three dimensions that is akin to a sponge-like morphology.

The power law slope (P_2) from the mesopore size regime (middle *q*, level 2) and the corresponding fractal dimensions are presented in Table 1. The mesoporous network of the starting biochar (0 min) exhibits as a pore fractal with a dimension of 2.8, displaying a branched and disordered network of smaller micropores [30]. After being gasified, the pore network of the CO_2 gasified biochar remains as a pore fractal with similar dimensions. In contrast, after 20 wt% of conversion (after 10 min), the fractal pore network in the H_2O and H_2O/CO_2 gasified biochars evolves into a surface fractal with dimension close to 3. This implies that the branched porous network breaks down and becomes dominated by mesopores with an extremely rough surface.

Table 1. Derived power law slope (P_2) from the mesopore size regime (middle q, level 2) and the corresponding fractal dimensions (D_p, D_s) for biochar gasified in H_2O, CO_2 and H_2O/CO_2 at 800°C for different times (0–50 min).

	0 min	10 min	20 min	30 min	40 min	50 min
H_2O						
P_2	2.8	3.3	3.3	3.1	3.0	3.4
Fractal dimension (± 0.05)	D_p = 2.8	D_s = 2.7	D_s = 2.7	D_s = 2.9	D_s = 3.0	D_s = 2.6
CO_2						
P_2	2.8	2.8	2.8	2.6	2.7	2.8
Fractal dimension (± 0.05)	D_p= 2.8	D_p = 2.8	D_p = 2.8	D_p = 2.6	D_p = 2.7	D_p = 2.8
H_2O/CO_2						
P_2	2.8	3.1	3.1	3.0	3.1	3.0
Fractal dimension (± 0.05)	D_p = 2.8	D_s = 2.9	D_s = 2.9	D_s = 3.0	D_s = 2.9	D_s = 3.0

A combination of the parameters from the micro- and mesopore size regimes provides a clearer picture of the pore network evolution. Fig. 6 provides a schematic diagram illustrating the evolution of pore network in biochar gasified in H_2O and CO_2. It should be noted that the pore network of H_2O/CO_2 gasified biochar evolves in a similar manner to H_2O gasified biochar and is not explicitly shown in Fig. 6. Also, the black areas in Fig. 6 (b) and (c) are adjusted to be similar to represent the similar carbon conversion. Before gas treatment, the biochar possesses a considerable fraction of pore channels (pore fractal) forming a network that criss-crosses the solid carbon framework (showed in black in Fig. 6a). The channels are formed from the aggregation of primary micropores with a radius of gyration R_{g1}. Therefore, the average channel width can be represented by the value of R_{g1} (4.2 ± 0.2 Å). Those branched channels are embedded in the solid and connected, forming a pore-fractal like network. The overall network is fractal at the mesoscopic length scale and the average size of the network (or cluster) has a radius of gyration R_{g2} (a correlation length that limits the extension of the order). Essentially, this network results in a sponge-like porous solid.

In the case of CO_2 gasification/activation (Fig. 6b), the pore network remains as a pore fractal over conversion, with a slight increase in the pore channel width (increase of R_{g1} from 4.2 to 5.4 ± 0.2 Å). A significant change is that the pore fractal regime extends to a larger length scale (power law scaling across a wider range of q, marked with dashed arrows), as indicated by the increase of R_{g2} (from 50 ± 2.5 to 266 ± 13.3 Å). Therefore, after 60 wt% of conversion in CO_2 results in an extended network of pores (larger clusters of pore channels). The average size of the new network of micropores (that clusters into a mesopore) is at least five times as large as that of the original one. The results indicate that CO_2 molecules tend to remove pore walls through the existing channels and extend the pore network. Hence, the local etching and collapse of pore walls is the main process during CO_2 gasification/activation. As a result, an extended network of branched micropore clusters is formed. It should be noted that the pore fractal could turn into surface fractal at a higher conversion level (after 50 min) when the channel walls break down to a point where they become part of a rough mesopore surface.

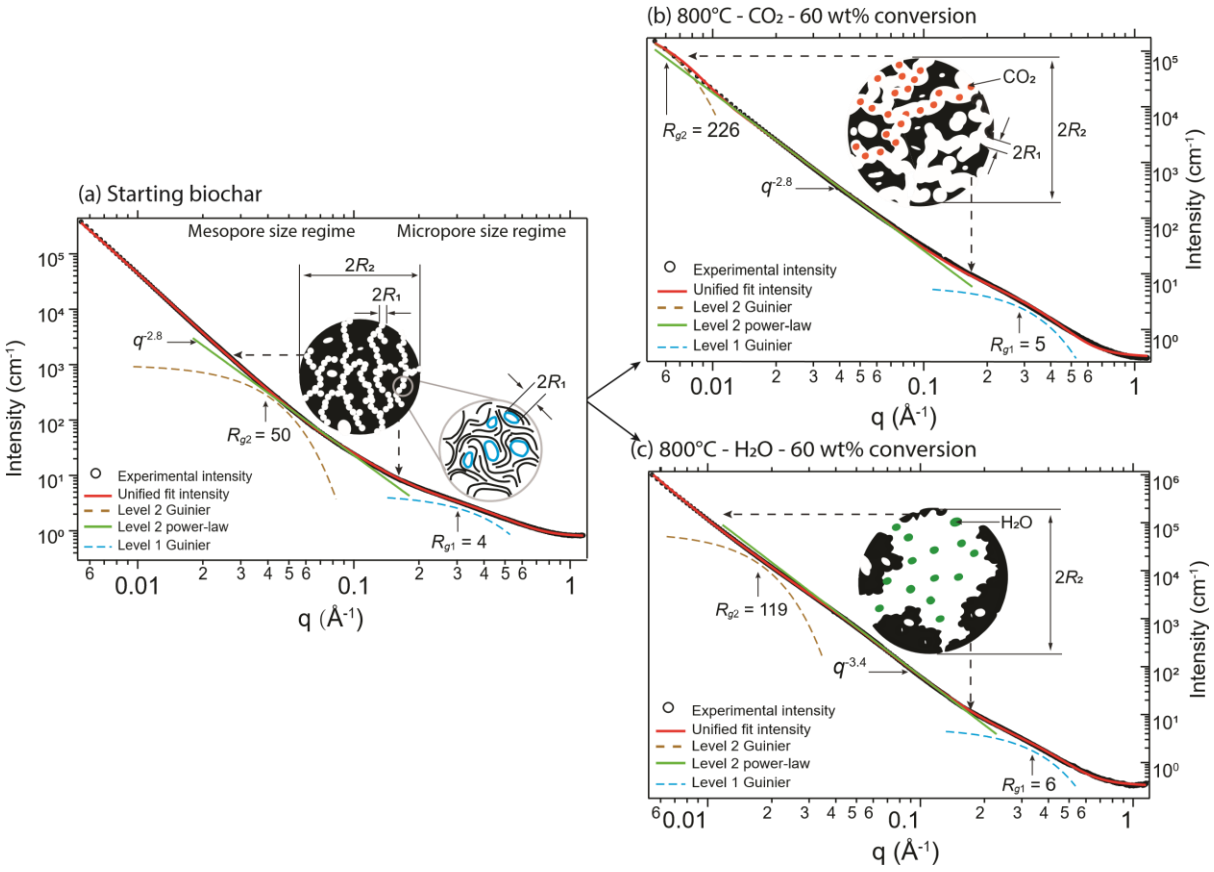

Fig. 6. Fitted SAXS patterns along with schematic representations of the fractal network in the mesopore size regime (middle *q*, level 2) for (a) biochar precursor, (b) biochar gasified in CO_2 to around 60 wt% conversion and (c) biochar gasified in H_2O to about 60 wt% conversion. The microstructural features on micro- and mesoscopic length scales are shown by R_{g1} and R_{g2} (± 0.5 Å). The dashed arrows indicate the symbolic range (the relative length scale of fractal network) of the respective power law regime at middle *q* (level 2). Note: the radius of pores can be calculated through $r = \sqrt{5/3}\ R_g$ if the pores are spherical.

In the case of H_2O gasification/activation (Fig. 6c), a slight increase in the micropore size (measured by R_{g1}) is also observed. More importantly, the pore network transforms from pore fractal to surface fractal with a dimension near 3, representing mesopores with extremely rough surfaces (consisting of an old network of micropores that has been etched into a larger mesopore). The average size of the mesopores (measured by R_{g2}) gradually

increases with the extension of biochar conversion. During the process, considerable solids are removed from the sponge-like clusters, leaving behind a larger mesopore with little solids across the pore (instead, showing rough surfaces, Fig. 6c). The mechanism could be the removal of layer after layer of carbon and/or the growth of pores of various sizes, giving rise to the collapse and destruction of channel walls. As a consequence, the widening of micropores into the mesopore range is more prevalent, explaining the more significant decrease in the micropore volume along with the higher mesopore volume for H_2O gasified biochar (Fig. 3). The results imply that carbon removal during gasification in H_2O is less selective than that in CO_2. H_2O molecules attack carbon sites in biochar located almost anywhere.

3.2.3. Correlations between the pore structure and the chemical structure of biochar

The SAXS data revealed that the evolutionary pathway of pore structure for H_2O gasified biochar is different from biochar gasified in CO_2. The differences become more significant after 40-50 wt% of conversion (30 min of reaction). Moreover, pore development in H_2O/CO_2 gasified biochar follows a similar pattern to H_2O gasified biochar. The pore evolution is either more selective (CO_2), resulting in larger networks of micropores, or less selective (H_2O), resulting in a breakdown of micropore clusters into mesopores. To have a better understanding of the correlation between the pore structure and the underlying carbon skeleton in biochar, the transformation of the carbon skeleton in biochar was also characterized using FT-Raman spectroscopy. Fig. 7a shows the changes of the band ratio $I_{(Gr+Vl+Vr)}/I_D$ with biochar conversion. Decreases in the band ratio indicate that small aromatic ring systems (less than 6 fused rings) are and preferentially consumed and/or converted to

larger ones [3]. During biochar gasification/activation, some atoms such as O are preferably removed, inducing the growth of the aromatic structures, presumably through a carbon re-combination process. However, judging from the band area ratio, it can be seen that the aromatic structures in H_2O gasified biochar change differently to those in CO_2 gasified biochar. This indicates differences in carbon sites preferably attacked by H_2O and CO_2 molecules, causing the different structural evolution of biochar under these gases. The aromatic structures in biochar gasified in H_2O/CO_2 and H_2O are similar, suggesting a reason why similar pathways of carbon removal are seen under H_2O/CO_2 and H_2O. The development of the pore structure produced by various gasifying agents is paralleled by the evolution of the aromatic structures characterized by Raman spectroscopy. Therefore, the evolution of the aromatic structures can be used as a guide to understanding the changes in the pore structure of biochar.

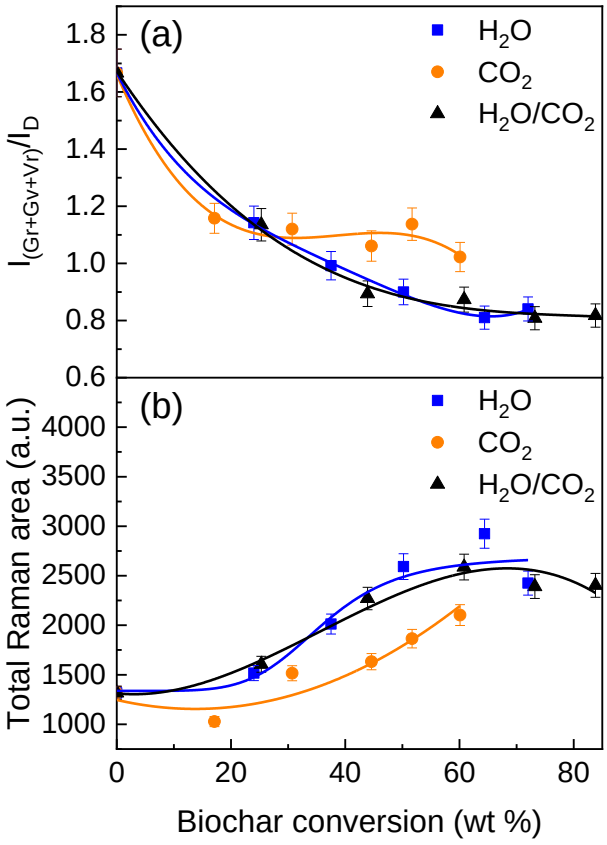

Fig. 7. Raman spectroscopic data. (a) the ratio of band areas $I_{(Gr+Vl+Vr)}/I_D$ and (b) the total Raman peak area (800 – 1800 cm^{-1}) of biochar as a function of biochar conversion.

The explanation for the differences in the porous structure of biochar developed by H_2O and CO_2 is complex. As stated before, pore structure evolvement in biochar is the result of the selective consumption of carbon atoms during gasification/activation. Therefore, the differences in the evolution of pore structure between H_2O and CO_2 gasified biochar is a result of the different selectivity in carbon consumption by each gas, which depends on variations in the reactivity between biochar with H_2O and CO_2.

One of the reasons for the different reactivity between H_2O-char and CO_2-char reactions could be the different reactivity of H_2O and CO_2 [13,14,53]. For a given temperature,

481 H_2O is more reactive than CO_2 as a higher energy is needed to dissociate a CO_2 molecule than
482 that for a H_2O molecule [13,14]. Thus, H_2O molecules are less selective than CO_2 molecules in
483 attacking carbon atoms. H_2O-char reactions would take place at an extensive number of active
484 sites whilst the active sites that are appropriate for CO_2-char reactions are limited.
485 Accordingly, H_2O molecules tend to interact with active sites located almost anywhere within
486 the porous structure. Whereas the local etching in existing pore channels is a more prevalent
487 process during gasification/activation with CO_2.

488 Another possible reason for the differences in carbon selectivity between H_2O and CO_2
489 could be related to the amount and properties of O-containing functional groups on the
490 biochar surface [16]. The continuous formation and decomposition of O-containing functional
491 groups is an important feature of gasification reactions [50]. Some of these O-containing
492 functional groups behave as reaction intermediates in gasification/activation processes.
493 Along the gasification/activation pathway, oxygen is firstly adsorbed on the carbon surface
494 and then removed along with the carbon atoms to which the oxygen is attached [16]. As the
495 process repeats, a certain degree of porosity in biochar is achieved. The evolution of the O-
496 containing functional groups in biochar was characterized using Raman spectroscopy [3] and
497 included in Fig. 7b. The content of O-containing functional groups is higher (indicated by the
498 higher total Raman area) in biochar produced by H_2O than CO_2. This is expected since the
499 reactivity of gases with biochar is associated with the amount of O-containing functional
500 groups [16,35,36,39]. When H_2O is used, more surface O-containing functional groups are
501 formed and a greater number of active sites are available for H_2O-char reactions to take place.
502 In other words, the elimination of carbon by H_2O would take place at more sites in the carbon
503 network. Whereas in CO_2, the lower content of O-containing functional groups limits where
504 carbon atoms can be extracted. The content of O-containing functional groups in biochar

produced in H_2O/CO_2 is nearly identical to that in H_2O gasified biochar, indicating that the process of carbon removal by H_2O could be the dominant process. This explains the similarity in how the pore structure evolves between biochar gasified in H_2O and H_2O/CO_2. Additionally, our previous work [39] found that different types of O-containing functional groups are formed in biochar during gasification with H_2O or CO_2. The different thermal stabilities of various O-containing functional groups could also be one of the reasons for the selective removal of carbon, as the relatively less stable O-containing functional groups would be decomposed first. Therefore, the amount and type of O-containing groups in biochar affect the selection of carbon atoms during gasification/activation reactions, thereby controlling the pathways of pore structure evolution and hence the final porosity developed.

Since the nature of gasification/activation lies in the selectivity of carbon consumption, it is reasonable to assume that gasifying agents tend to attack the relatively more reactive and less stable structures. Accordingly, the weak pore walls would be removed in preference to the relatively strong walls. As carbon conversion proceeds, the selectivity for the remnant structures by H_2O and CO_2 would become more pronounced as they become, on average, more stable and less reactive.

3.3. Effects of temperature and biomass particle sizes on the pore structure of biochar

Fig. 8 shows some major pore structure parameters acquired from SAXS measurements for biochar gasified at different temperatures for 4 min (biochar B). Overall, the increase of temperature gives rise to a significant increase in SSA and pore volume as the biochar conversion increases, especially the mesopore volume, irrespective of the type of gasifying agent. It seems that the development of both micro- and mesopores is enhanced

with increasing temperature. This could be attributed to the enhanced thermal breakdown and the higher reaction rate at higher temperature, leading to a higher level of biochar conversion. The average size of micro- and mesopores are similar for biochars gasified at different temperatures. Moreover, when the temperature increased from 700 to 900 ˚C where similar biochar conversion were reached (7% and 8% of char yield were obtained for biochar gasified in CO_2 and H_2O), the values of micro- and mesopore volumes produced by H_2O and CO_2 become more similar. The decreased differences in porosity development between H_2O and CO_2 gasified biochar suggests that the differences in carbon removal by H_2O and CO_2 becomes less significant at higher temperature. At an elevated temperature, the reaction rate of carbon sites with H_2O or CO_2 increases rapidly especially for those carbon sites with higher activation energies [5]. When different carbon sites have closer gasification rates, carbon removal become less selective. As a result, the differences in the pore structure of biochar produced by H_2O and CO_2 become smaller.

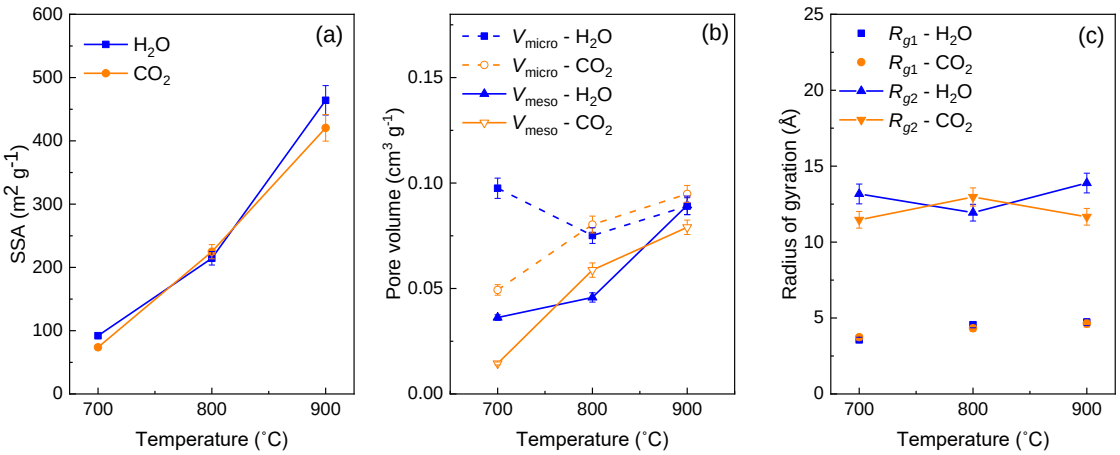

Fig. 8. SAXS derived (a) SSA, (b) pore volume and (c) radius of gyration for biochar gasified in H_2O (closed symbols) and CO_2 (open symbols) at different temperatures (700, 800 and 900 ˚C).

Fig. 9 shows the SAXS curves of biochar samples prepared from Mallee wood with various particle sizes (biochar C). As expected, for gasification both in H_2O and CO_2, little change in the SAXS patterns among different biomass particle sizes is observed. This demonstrates that the biomass particle size has almost no effect on the pore structure development. In our previous study [40], the Raman characterization of samples with different particle sizes revealed that there is no significant changes in the aromatic ring systems and the content of O-containing functional groups in biochar. The results, therefore, again confirm that the evolution of pore structure in biochar is closely linked to the changes in the aromatic ring systems and the O-containing functional groups. The gasifying agents and gasification temperature are the most important in defining the gasification reactions and processes rather than bulk particle size of biomass feedstock.

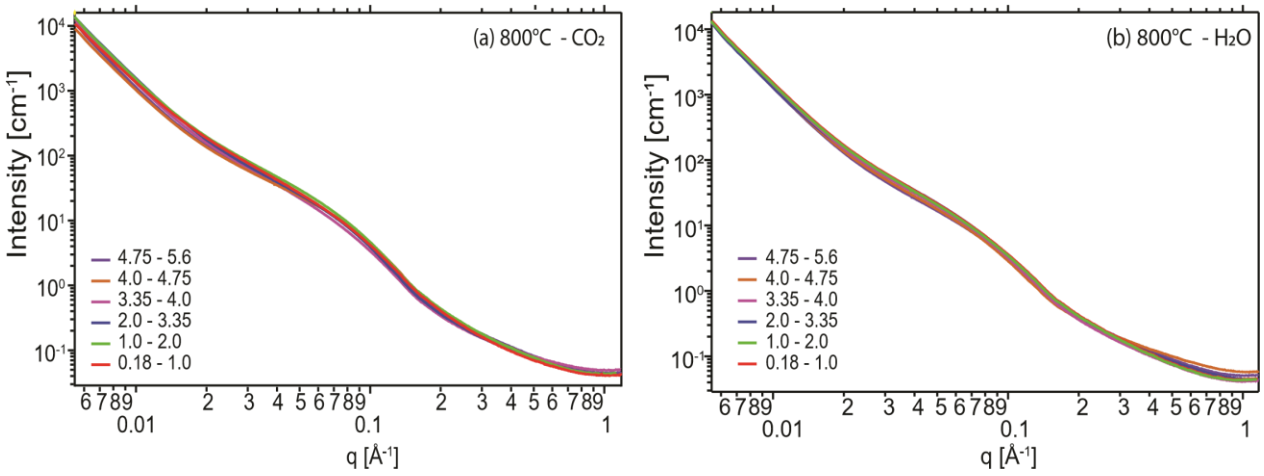

Fig. 9. SAXS curves of biochar gasified in (a) CO_2 and (b) H_2O with biomass of different particle sizes (mm).

4. Conclusions

The evolution of the pore structure in biochar during gasification/activation in H_2O, CO_2 and H_2O/CO_2 was investigated using SAXS. Under the experimental conditions used in this work, the overall pore development in H_2O/CO_2 gasified biochar is akin to that in H_2O gasified biochar. The CO_2 activated biochars display pore fractal features (representing a network of branched micropore clusters) in the mesopore size regime up to a 60 wt% conversion. An increase in conversion level gives rise to a remarkable growth in the size of the pore fractal network. Whereas for the H_2O gasified biochar, the mesoporous network is dominated by mesopores with extremely rough surfaces after 10 min gasification (conversion level higher than 20 wt%), presenting as surface fractals, rather than networks of micropores. The development of the pore structure produced by various gasifying agents is paralleled by the evolution of the aromatic structures characterized by Raman spectroscopy. The different porous structure of biochar from H_2O and/or CO_2 gasification/activation is a consequence of the differences in carbon removal by H_2O and CO_2, which is determined by the reactivity of various carbon sites with H_2O and CO_2. Carbon removal in biochar is less selective when gasified with H_2O than with CO_2. This could be due to the higher content of O-containing functional groups in H_2O gasified biochar, together with higher reactivity of H_2O. Besides, the differences in pore structure, caused by H_2O and CO_2, decreases at higher temperature. The pore structure of biochar is barely affected by the biomass particle sizes.

Acknowledgements

This work received funding from the Australian Research Council (DP180101788, FT160100303, LE140100075). The project is also supported by the Australian Government through ARENA's Emerging Renewables Program. This research was undertaken on the SAXS beamline at the Australian Synchrotron, part of ANSTO. We wish to thank Li Dong, Yao Song and Shu Zhang providing biochar sample.

References

[1] Li C-Z. Special issue—gasification: a route to clean energy. Process Saf Environ Prot 2006;84:407–8.

[2] Sikarwar VS, Zhao M, Clough P, Yao J, Zhong X, Memon MZ, Shah N, Anthony EJ, Fennell PS. An overview of advances in biomass gasification. Energy Environ Sci 2016;9:2939–77.

[3] Li X, Hayashi J-I, Li C-Z. Volatilisation and catalytic effects of alkali and alkaline earth metallic species during the pyrolysis and gasification of Victorian brown coal. Part VII. Raman spectroscopic study on the changes in char structure during the catalytic gasification in air. Fuel 2006;85:1509–17.

[4] Foster MD, Jensen KF. SAXS investigation of model carbon pore structure and its change with gasification. Carbon N Y 1991;29:271–82.

[5] Liu Y, Paskevicius M, Sofianos MV, Parkinson G, Li C-Z. In situ SAXS studies of the pore development in biochar during gasification. Carbon N Y 2020;172.

[6] Qian K, Kumar A, Zhang H, Bellmer D, Huhnke R. Recent advances in utilization of

608 biochar. Renew Sustain Energy Rev 2015;42:1055–64.

609 [7] Hurt RH, Sarofim AF, Longwell JP. Effect of Nonuniform Surface Reactivity on the
610 Evolution of Pore Structure and Surface-Area During Carbon Gasification. Energy &
611 Fuels 1991;5:463–8.

612 [8] Gibaud A, Xue JS, Dahn JR. A small angle X-ray scattering study of carbons made from
613 pyrolyzed sugar. Carbon N Y 1996;34:499–503.

614 [9] McEnaney B, Mays TJ. Chapter 5 – Porosity in Carbons and Graphites. Butterworth &
615 Co. (Publishers) Ltd; 1989.

616 [10] Guizani C, Jeguirim M, Gadiou R, Escudero Sanz FJ, Salvador S. Biomass char
617 gasification by H_2O, CO_2 and their mixture: Evolution of chemical, textural and
618 structural properties of the chars. Energy 2016;112:133–45.

619 [11] Coetzee GH, Sakurovs R, Neomagus HWJP, Morpeth L, Everson RC, Mathews JP, Bunt
620 JR. Pore development during gasification of South African inertinite-rich chars
621 evaluated using small angle X-ray scattering. Carbon N Y 2015;95:250–60.

622 [12] Rodríguez-Reinoso F. Controlled gasification of carbon and pore structure
623 development. In: Lahaye J. EP, editor. Fundam. Issues Control Carbon Gasif. React.,
624 Springer, Dordrecht; 1991, p. 533–71.

625 [13] González JF, Román S, González-García CM, Nabais JMV, Ortiz AL. Porosity
626 development in activated carbons prepared from walnut shells by carbon dioxide or
627 steam activation. Ind Eng Chem Res 2009;48:9354.

628 [14] Rodríguez-Reinoso F, Molina-Sabio M, González MT. The use of steam and CO_2 as
629 activating agents in the preparation of activated carbons. Carbon N Y 1995;33:15–23.

[15] Pastor-Villegas J, Durán-Valle CJ. Pore structure of activated carbons prepared by carbon dioxide and steam activation at different temperatures from extracted rockrose. Carbon N Y 2002;40:397–402.

[16] Molina-Sabio M, González MT, Rodriguez-Reinoso F, Sepúlveda-Escribano A. Effect of steam and carbon dioxide activation in the micropore size distribution of activated carbon. Carbon N Y 1996;34:505–9.

[17] Arenas E, Chejne F. The effect of the activating agent and temperature on the porosity development of physically activated coal chars. Carbon N Y 2004;42:2451–5.

[18] Ostafiychuk BK, Mandzyuk VI, Kulyk YO, Nagirna NI. SAXS investigation of nanoporous structure of thermal-modified carbon materials. Nanoscale Res Lett 2014;9:160.

[19] Alcañiz-Monge J, Cazorla-Amorós D, Linares-Solano A, Yoshida S, Oya A. Effect of the activating gas on tensile strength and pore structure of pitch-based carbon fibres. Carbon N Y 1994;32:1277–83.

[20] Wigmans T. Industrial aspects of production and use of activated carbons. Carbon N Y 1989;27:13–22.

[21] Walker PL. Production of activated carbons: use of CO_2 versus H_2O as activating agent. Carbon N Y 1996;34:1297–9.

[22] Pastor AC, Marsh H. Preparation of activated carbon cloths from viscous rayon. Part II : physical activation processes. Carbon N Y 2000;38:379–95.

[23] Wang Y, Liu R. Comparison of characteristics of twenty-one types of biochar and their ability to remove multi-heavy metals and methylene blue in solution. Fuel Process Technol 2017;160:55–63.

[24] Chavez Panduro EA, Beuvier T, Fernández Martínez M, Hassani L, Calvignac B, Boury F, Gibaud A. Small-angle X-ray scattering analysis of porous powders of CaCO3. J Appl Crystallogr 2012;45:881–9.

[25] Okolo GN, Everson RC, Neomagus HWJPJP, Roberts MJ, Sakurovs R. Comparing the porosity and surface areas of coal as measured by gas adsorption, mercury intrusion and SAXS techniques. Fuel 2015;141:293–304.

[26] Brenner AM, Adkins BD, Spooner S, Davis BH. Porosity by small-angle X-ray scattering (SAXS): comparison with results from mercury penetration and nitrogen adsorption. J Non Cryst Solids 1995;185:73–7.

[27] Bahadur J, Medina CR, He L, Melnichenko YB, Rupp JA, Blach TP, Mildner DFR. Determination of closed porosity in rocks by small-angle neutron scattering. J Appl Crystallogr 2016;49:2021–30.

[28] Härk E, Petzold A, Goerigk G, Risse S, Tallo I, Härmas R, Lust E, Ballauff M. Carbide derived carbons investigated by small angle X-ray scattering: Inner surface and porosity vs. graphitization. Carbon N Y 2019;146:284–92.

[29] Pfeifer P. Fractal dimension as working tool for surface-roughness problems. Appl Surf Sci 1984;18:146–64.

[30] Pfeifer P, Ehrburger-Dolle F, Rieker TP, González MT, Hoffman WP, Molina-Sabio M, Rodríguez-Reinoso F, Schmidt PW, Voss DJ. Nearly space-filling fractal networks of carbon nanopores. Phys Rev Lett 2002;88:115502.

[31] Bale HD, Schmidt PW. Small-Angle X-Ray-Scattering Investigation of Submicroscopic Porosity with Fractal Properties. Phys Rev Lett 1984;53:596–9.

[32] Beaucage G, IUCr. Small-Angle Scattering from Polymeric Mass Fractals of Arbitrary Mass-Fractal Dimension. J Appl Crystallogr 1996;29:134–46.

[33] Beaucage G. Determination of branch fraction and minimum dimension of mass-fractal aggregates. Phys Rev E - Stat Physics, Plasmas, Fluids, Relat Interdiscip Top 2004;70:10.

[34] Reich MH, Russo SP, Snook IK, Wagenfeld HK. The application of SAXS to determine the fractal properties of porous carbon-based materials. J Colloid Interface Sci 1990;135:353–62.

[35] Liu Y, Paskevicius M, Wang H, Parkinson G, Veder JP, Hu X, Li C-Z. Role of O-containing functional groups in biochar during the catalytic steam reforming of tar using the biochar as a catalyst. Fuel 2019;253:441–8.

[36] Liu Y, Paskevicius M, Wang H, Fushimi C, Parkinson G, Li C-Z. Difference in tar reforming activities between biochar catalysts activated in H_2O and CO_2. Fuel 2020;271:117636.

[37] Advanced biomass gasification technology, Australian Renewable Energy Agency n.d.

[38] Grinding pyrolysis, Renergi Pty Ltd. http://www.renergi.net/grinding_pyrolysis. (accessed December 20, 2020).

[39] Wang S, Wu L, Hu X, Zhang L, O'Donnell KM, Buckley CE, Li C-Z. An X-ray photoelectron spectroscopic perspective for the evolution of O-containing structures in char during gasification. Fuel Process Technol 2018;172:209–15.

[40] Wang S, Wu L, Hu X, Zhang L, Li T, Li C-Z. Effects of the particle size and gasification atmosphere on the changes in the char structure during the gasification of mallee

biomass. Energy and Fuels 2018;32:7678–84.

[41] Kirby NM, Mudie ST, Hawley AM, Cookson DJ, Mertens HDT, Cowieson N, Samardzic-Boban V. A low-background-intensity focusing small-angle X-ray scattering undulator beamline. J Appl Crystallogr 2013;46:1670–80.

[42] Dreiss CA, Jack KS, Parker AP. On the absolute calibration of bench-top small-angle X-ray scattering instruments: A comparison of different standard methods. J Appl Crystallogr 2006;39:32–8.

[43] Spalla O, Lyonnard S, Testard F. Analysis of the small-angle intensity scattered by a porous and granular medium. J Appl Crystallogr 2003;36:338–47.

[44] SAXS Software - scatterBrain.

[45] Beaucage G. Approximations leading to a unified exponential power-law approach to small-angle scattering. J Appl Crystallogr 1995;28:717–28.

[46] Ilavsky J, Jemian PR. Irena : tool suite for modeling and analysis of small-angle scattering. J Appl Crystallogr 2009;42:347–53.

[47] Hurd AJ, Schaefer DW, Smith DM, Ross SB, Le Méhauté A, Spooner S. Surface areas of fractally rough particles studied by scattering. Phys Rev B 1989;39:9742–5.

[48] Paskevicius M. A nanostructural investigation of mechanochemically synthesised hydrogen storage materials, PhD thesis, Curtin University of Technology, Australia. 2009.

[49] Román S, González JF, González-García CM, Zamora F. Control of pore development during CO_2 and steam activation of olive stones. Fuel Process Technol 2008;89:715–

717 20.

718 [50] Marsh H, Rodríguez-Reinoso F. CHAPTER 5 - Activation Processes (Thermal or
719 Physical). In: Marsh H, Rodríguez-Reinoso FBT-AC, editors. Act. Carbon, vol. 2,
720 Elsevier Science & Technology Books; 2006, p. 243–321.

721 [51] Marsh H, Rodríguez-Reinoso F. CHAPTER 2 - Activated Carbon (Origins). In: Marsh H,
722 Rodríguez-Reinoso FBT-AC, editors. Act. Carbon, Oxford: Elsevier Science &
723 Technology Books; 2006, p. 13–86.

724 [52] Jafta CJ, Petzold A, Risse S, Clemens D, Wallacher D, Goerigk G, Ballauff M. Correlating
725 pore size and shape to local disorder in microporous carbon : A combined small angle
726 neutron and X-ray scattering study. Carbon N Y 2017;123:440–7.

727 [53] González JF, Encinar JM, González-García CM, Sabio E, Ramiro A, Canito JL, Gañán J.
728 Preparation of activated carbons from used tyres by gasification with steam and
729 carbon dioxide. Appl Surf Sci 2006;252:5999–6004.

730
731
732
733
734
735
736
737
738
739
740
741